UC Santa Barbara

UC Santa Barbara Previously Published Works

Title

Precipitation and hardening in irradiated low alloy steels with a wide range of Ni and Mn compositions

Permalink

Authors

Almirall, N
Wells, PB
Yamamoto, T
et al.

Publication Date

DOI

Peer reviewed

Precipitation and Hardening in Irradiated Low Alloy Steels with a Wide Range of Ni and Mn Compositions

N. Almirall[1], P.B. Wells[1], T. Yamamoto[1], K. Wilford[2], T. Williams[2], N. Riddle[2] and G.R. Odette[1]

[1]University of California, Santa Barbara

[2]Rolls-Royce

Corresponding Author

G. Robert Odette
Distinguished Research Professor Emeritus, UCSB Mechanical Engineering and Materials Departments
Email: odette@engineering.ucsb.edu
Phone: (805) 964-5586
Fax: (805) 893-8651
Address:
Mechanical Engineering
2355 Engineering II
University of California, Santa Barbara
Santa Barbara, CA 93106-5070

Abstract

Mn-Ni-Si intermetallic precipitates (MNSPs) that are observed in some Fe-based alloys following thermal aging and irradiation are of considerable scientific and technical interest. For example, large volume fractions (f) of MNSPs form in reactor pressure vessel low alloy steels irradiated to high fluence, resulting in severe hardening induced embrittlement. Nine compositionally-tailored small heats of low Cu RPV-type steels, with an unusually wide range of dissolved Mn (0.06-1.34 at.%) and Ni (0.19-3.50 at.%) contents, were irradiated at $\approx 290°C$ to $\approx 1.4 \times 10^{20}$ n/cm^2 at an accelerated test reactor flux of $\approx 3.6 \times 10^{12}$ n/cm^2-s (E > 1 MeV). Atom probe tomography shows Mn-Ni interactions play the dominant role in determining the MNSP f, which correlates well with irradiation hardening. The wide range of alloy compositions results in corresponding variations in precipitates chemistries that are reasonably similar to various phases in the Mn-Ni-Si projection of the Fe based quaternary. Notably, f scales with $\approx Ni^{1.6}Mn^{0.8}$. Thus f is modest even in advanced high 3.5 at.% Ni steels at very low Mn (Mn starvation); in this case Ni-silicide phase type compositions are observed.

Key Words: Pressure Vessel Steels; Radiation Damage; Atom Probe Tomography; Nano-Scale Precipitates; Irradiation Embrittlement

1. Introduction

Formation of nm-scale Mn-Ni-Si precipitates (MNSPs), like the G-phase, is observed in a number of Fe-based alloys, during long-time, intermediate temperature thermal aging, as well as in under irradiation [1–4]. Recently, precipitation of an ultrahigh density of Ti-Ni-Si G-phase precipitates, with Ti replacing Mn, was used to create very high strength steels [5]. However, there is little experimental insight on the alloy Mn-Ni-Si dependence of the MNSP number densities (N), sizes (d), volume fractions (f), chemistries and crystallographic phases. Here we characterize a matrix of nine compositionally tailored low Cu steels, with systematically varying dissolved Ni (0.19-3.50 at.%) and Mn (0.06-1.34 at.%) contents, at an approximately constant 0.44 ± 0.05 at.% Si. Note the square root of the f of MNSPs largely controls hardening and embrittlement [6,7]. Thus, the primary objective of this study is to provide fundamental insight on the Mn-Ni dependence of N, d, f, and MNSP composition and the corresponding effect on irradiation hardening ($\Delta\sigma_y$).

One application of this work, relates to the extended operation of light water reactors for 80 years, which is needed to sustain nuclear power as a carbon-free energy source [8]. Life extension will require ensuring the integrity of the massive thick-walled reactor pressure vessels (RPV) in the face of neutron irradiation embrittlement. Embrittlement is manifested as upward ductile-to-brittle transition temperature shifts. The primary cause of embrittlement is irradiation hardening, characterized by $\Delta\sigma_y$ [9–14]. As described in the cited papers, neutrons create high-energy primary recoil atoms that produce excess vacancies and self-interstitial defects in displacement cascades [15]. The diffusion, clustering and annihilation of these defects lead to: a) formation of defect-solute complexes; and, b) radiation enhanced solute diffusion (RED) precipitation [9–14]. Note, radiation induced segregation also plays a role in MNSP nucleation, especially at lower solute contents [16–20]. The nano-scale precipitates and defect clusters result in hardening ($\Delta\sigma_y$) by acting as dispersed obstacles to dislocation glide. Hardening results in embrittlement by increasing the temperature at which the blunting crack tip field can reach the critical stress and volume for cleavage fracture [21–24]. Thus understanding these microstructural evolutions under irradiation as a function of the neutron fluence (ϕt, n/cm^2), flux (ϕ, n/cm^2-s), irradiation temperature (T_i), alloy composition (Cu, Ni, P, .. in at.%) and start of life microstructure, is required to develop robust, physically-based predictive hardening and embrittlement models, like that developed by Ke et al.[25]; and the reduced order formulation proposed by Eason, Odette, Nanstad and Yamamoto (EONY) fitted to the surveillance embrittlement database on embrittlement [26].

The RPV embrittlement issue has been recognized since the beginning of light water reactor service, and pressure vessel surveillance capsules and testing have been required, starting with the first fully commercial pressurized water reactor, Yankee Rowe. Embrittlement as a research topic published in the open literature has a long history, beginning in the mid-1960s at the Naval Research Laboratory [27]. The first paper identifying and modeling the primary RPV steel embrittlement mechanism as being RED acceleration of the formation of Cu-rich precipitates (CRPs) was published in 1983 [13]. Subsequently, a worldwide research effort, continuing to this day, has led to the following set of conclusions. Note, only a few references are given as key examples.

As well as Cu, Ni plays a major role in embrittlement and is enriched in CRPs, along with Mn and Si [14].

Ni-Mn-Si precipitates (MNSPs) form at high fluence even in the absence of Cu, typically as G ($Ni_{16}Mn_8Si_7$) and Γ_2 (Ni_3MnSi)-type phases [28,29].

The MNSPs mostly evolve from precursor defect solute-cluster complexes formed by segregation of solutes to small dislocation loops formed in displacement cascades [25,28].

In the presence of Cu, the MNSPs first form a shell around CRPs at low fluence, and subsequently evolve as appendages on CRPs at higher fluence [28,30].

Hardening and embrittlement are approximately proportional to the square root of the precipitate volume (or mole) fraction (f) [6,7].

Since typical RPV steels contain Mn + Ni + Si as alloying elements in much higher concentrations (usually > 2%), compared to dissolved impurity Cu (< 0.3%), the resulting volume fraction of MNSPs, f, and the corresponding $\Delta\sigma_y$ and embrittlement, are potentially much larger than for CRPs alone, but only at sufficiently high fluence [28].

MNSPs are not explicitly accounted for in current US regulatory embrittlement models, that are based on lower fluence RPV surveillance data [26]. Notably, these models underpredict high fluence (and flux) test reactor data [11].

The results reported here are for a small subset of data from the UCSB ATR-2 irradiation experiment, involving a large matrix of 172 alloys irradiated to high ϕt over a range of T_i. The objective of the UCSB ATR-2 study is to evaluate and model: a) the formation of and hardening by CRPs, MNSPs and solute cluster complexes at high ϕt, pertinent to the extended nuclear plant life of 80 years, or more; and, b) the effects of dose rate, as a basis to extrapolate the $\approx 290°C$, intermediate ϕ ($\approx 3.6x10^{12}$ n/cm^2-s) ATR-2 irradiation results to low ϕ vessel service conditions ($\approx 4x10^{10}$ n/cm^2-s). Here, we use atom probe tomography (APT) to characterize the MNSPs and tensile (and, or shear punch and microhardness) tests to measure the corresponding $\Delta\sigma_y$. The data, newly reported here, is for a subset of 9 steels, selected from a new compositionally tailored low alloy series, with systematic Ni and Mn variations that are much wider than previously studied [31]. The alloys were selected from a total of 50 steel compositions, which we call the Advanced Steel Matrix (ASM) for reasons described below. The matrix of nine steels provides a clean and quantitative basis to evaluate the effects of Ni-Mn interactions on MNSPs, and the corresponding $\Delta\sigma_y$ in steels with compositions that are otherwise similar. Specifically, we explore and quantify the hypothesis that large reductions in the alloy Mn content to 0.3%, or less (typically Mn concentrations are more than 0.8%), can suppress the formation of MNSPs sufficiently to compensate for high $\approx 3.5\%$ Ni [32].

An immediate practical motivation for this work is that such high Ni steels have outstanding unirradiated strength and toughness properties [32–36]. As a specific example, the A508 Gr. 4N steel, with > 3.2% Ni, has a room temperature yield stress that is typically $\approx 25\%$ higher than for A508 Gr. 3 with $\approx$ 0.6%Ni. The corresponding master curve fracture toughness 100 MPa$\sqrt{m}$ reference temperature, T_o, is lower, with typical values -140°C, compared to -90°C (or higher) for Gr. 3 steels. The improved properties are associated with smaller prior austenitic grains and carbides, and finer martensitic-bainitic lath and packet structures. The corresponding Mn contents are typically $\approx 0.3\%$ versus 1.5% for A508 Gr. 4N and Gr. 3, respectively. The lower Mn in Gr. 4N reduces the irradiation hardening and embrittlement sensitivity, so as to offset the effect of high Ni. To compensate for low Mn, it is important to keep the S and other impurities low. Thus for RPV applications, A508 Gr. 4N is part of an alloy class known as "superclean" steels. Practical issues aside, the fundamental scientific objective of this work was to probe and quantify Ni-Mn interactions in terms of the MNSP characteristic N, d, f, compositions and their associations with other microstructural features, and their effects on the corresponding irradiation hardening.

In summary, the results show that: a) f and $\Delta\sigma_y$ decrease with decreasing Mn at all Ni levels; b) at very low Mn and high, to very high, Ni, the observed precipitate chemistries are not close to those for G or Γ_2 phases and Ni-silicide type compositions are the observed alternative, leading to lower f due to Mn starvation; c) the MNSP f correlates well with an empirical chemistry factor of Ni$^{1.6}$Mn$^{0.8}$, quantifying the effect of Mn starvation at ≈ 0.4 at.% Si; d) at a specified Ni content, the MNSP Si/Mn ratio decreases with increasing Mn, demonstrating the trade-off between these elements; and, e) $\Delta\sigma_y$ correlates well with the $\sqrt{f}$.

2. Materials and Methods

2.1 Alloys and Irradiations

The UCSB ATR-2 experiment was designed to investigate embrittlement at extended life fluences at intermediate flux of 3.6×10^{12} n/cm^2-s for T_i from 250 to 310°C. The peak ATR-2 flux is $\approx$ 90 times than that experienced by an in-service vessel. The ATR-2 alloy matrix includes $\approx$ 172 RPV alloys, in several sample geometries, yielding a total of $\approx$ 1600 specimens. The ASM, supplied by Rolls Royce, is comprised of 55 new split-melt advanced steels, spanning 50 compositions and an additional 5 heat treatments on selected alloys. All the alloys were irradiated in ATR-2 in the form of 20 mm diameter, 0.5 mm thick disc multipurpose coupons, along with 62 alloys in the form of subsized SS-J2 16 x 4 x 0.5 mm tensile specimens. The primary focus of this paper is on the APT characterization of 9 ASM steels neutron irradiated to $\approx 1.4 \times 10^{20}$ n/cm^2 at $\approx$ 290°C. The bulk alloy compositions are given in Table 1 (in at.%), along with the baseline heat treatment.

Table 1. Nominal steel compositions (at.%)

Alloy	Bulk at%								
	Cu	Ni	Mn	Si	Cr	Mo	P	C	Fe
R1	0.05	0.28	0.26	0.41	0.11	0.28	0.009	0.97	Bal.
R17	0.05	3.26	1.52	0.39	0.11	0.29	0.005	1.06	Bal.
R19	0.05	1.57	0.26	0.39	0.14	0.30	0.014	1.06	Bal.
R22	0.05	1.58	1.51	0.41	0.11	0.30	0.011	1.34	Bal.
R26	0.04	3.29	0.25	0.37	0.11	0.30	0.016	1.20	Bal.
R34	0.06	3.25	0.08	0.38	0.10	0.30	0.011	1.02	Bal.
R35	0.05	0.22	1.51	0.41	0.12	0.28	0.012	1.24	Bal.
R39	0.03	0.66	1.47	0.41	0.12	0.28	0.007	0.97	Bal.
R48	0.06	3.29	0.77	0.41	0.11	0.29	0.005	1.29	Bal.

Austenitized at 920°C for 1 h followed by an air cool, then tempered at 600°C for 5 h followed by an air cool.

2.2 Precipitate Characterization

Atom probe tomography (APT) is a well-known, high-resolution microscopy technique which provides information on the atomic positions and chemical identity in the extremely small volume of a needle shaped tip, with a typical hemispherical radius of $\approx$ 50 nm and $\approx$ 500 nm length. APT is an extremely powerful tool for characterizing the high number density of nm-scale precipitates in irradiated RPV steels. We refer the reader to details of the APT technique described in several outstanding books [37,38] and numerous journal papers, for example [39–41]. Field evaporation of ions from the sharp needle tip, subject to enormous local electric field gradients of tens of V/nm, is driven by a combination of a high standing potential and precisely timed, high frequency voltage or laser pulses. An ion is field emitted on the order of one in every 100 pulses. The ion position in the tip is determined by back projection from a 2D position sensitive detector site, with a wide field of view; the isotope species is determined by the corresponding time of flight.

Multiple field evaporations of various alloy constituents produce a spectrum of flight times that are directly related to the ion's mass to charge ratio (MCR). Sharp peaks in the MCR spectrum mark a particular isotope and charge state. Note the ^{58}Ni^{+2} and ^{58}Fe^{+2} peaks overlap, hence it is necessary to deconvolute the contributions of these two elements. Since this peak contains 68.01% of all naturally occurring Ni and

0.28% of all the corresponding Fe, it is initially ranged to be Ni. After the solute clusters have been identified, a correction is made to the number of Fe and Ni atoms using abundance ratios for other Ni and Fe isotopes. This correction results in a slightly reduced Ni content in the bulk, matrix and solute clusters relative to the initial ranging of the mass spectrum. There is sufficient Ni in the bulk (0.19-3.50 at.%) to warrant this correction. Note, some studies have neglected the $^{58}Ni^{+2}$ and $^{58}Fe^{+2}$ peak in the initial cluster identification step [42,43]. However, depending on the algorithm used, this method leads to large underestimates of the cluster size and volume fraction, since it misses a large fraction of the Ni actually present. This is the case for the Integrated Visualization and Analysis Software (IVAS) maximum separation distance algorithm.

The sequence of detector ion hit x, y positions is recoded for subsequent 3D reconstruction. The z position, in the tip axis direction, assumes a uniform erosion of atoms due to ion emissions from a smooth hemispherical tip surface. Typical APT runs detect to 10^6 to 10^7 ion counts at an efficiency (ions detected to ions field evaporated) that depends on the APT tool, but ranges from $\approx 37\%$, as in this case, to 80%. The overall results of an APT run depend on many factors such as the tip temperature, voltage versus laser pulsing, the time-position dependent geometry of the tip as it erodes, including deviations from a hemispherical geometry, and the details of the particular microstructure under study.

The recorded x, y, z isotope positions are reconstructed by proprietary post processing codes like the IVAS (3.6.12), which was used in this work. There are a large number of assumptions in the standard reconstruction algorithms, like the uniform erosion of the tips and the assumed shape evolution of its shape as a perfect hemisphere. Further, the results are sensitive to the method and parameterization of analyzing the precipitates in terms of their number densities, sizes, shapes, mole fractions and compositions. Note, precipitate compositions typically vary spatially in a complex manner, like core-shell and precipitate appendage structures [30]. Finally, APT is subject to a number of artifacts such as surface diffusion, chromatic aberrations, multiple hits, pre-emission and variations in the local magnification factor [2,44–47]. The latter is a particularly important issue, since favored, lower evaporation potential emission of certain less strongly bound elements changes the local topology of the tip. Precipitates with lower evaporation potentials than the matrix result in local flattening, or dimpling, of the tip; and in more complex cases even selective evaporation of parts of the precipitate itself [2,48]. The local changes in tip topology lead to trajectory aberrations (TA), which change the local magnification factor, and can cause evaporated matrix atoms to appear as though they are part of the precipitates. The effects of TA increase with decreasing precipitate size and generally lead to a precipitate-matrix mixing zone artifact over a length scale of ≈ 1 to > 2 nm [49]. In this work, the precipitate diameters average only ≈ 2.4 nm, thus we assume that the Fe content indicated by a standard IVAS analysis is a TA and reconstruction artifact. Both STEM-EDS and multi technique characterization studies (small-neutron scattering, temperature dependent small angle magnetic neutron scattering, small-angle X-ray scattering, positron annihilation coincidence Doppler broadening orbital electron momentum spectrum measurements and combined electrical resistivity and Seebeck coefficient measurements) have all clearly shown that high concentrations of Fe in the precipitates is an APT artifact [2,47].

The APT analyses were performed using the 3000X HR Local Electrode Atom Probe (LEAP) at the University of California Santa Barbara (UCSB), and a 4000X HR LEAP at the Idaho Center for Advanced Energy Studies (CAES). The APT tips were prepared by standard Focused Ion Beam liftout and annular milling methods to form a tip radius of 50-100 nm. The FIB voltages and beam currents were reduced to 5 kV and 48 pA and 2 kV and 27 pA for final cleanup steps and removal of Ga damage layer [50]. APT was performed in voltage mode with a tip temperature of 50K, a pulse fraction of 20%, an ion detection rate of 0.50%, and a pulse repetition rate of 200 kHz. The residual Ga-ion damage region was excluded from the analysis.

IVAS cluster analysis maximum separation algorithms were used to determine the number density (N), size distribution, average diameter (<d>), volume fraction (f) and compositions of the precipitates.

Fine-tuning of the image compression factor and k-value was required to reach an accurate planar d spacing, identified by low-index crystallographic poles, such as (110) and (200). The dataset image compression factor ranged between 1.50 and 1.65 and the k-value between 2.7 and 5.2. The maximum separation method was used to distinguish the clustered solutes from those in the surrounding matrix [51,52].

The key cluster analysis parameters are a maximum separation distance to define a solute atom (Ni, Mn, Si, Cu, P) as being part of a cluster (d_{max}) and a minimum number of solute atoms that defines a cluster (N_{min}). Notably, the results of the cluster analysis can be strongly influenced by these parameters [53]. A d_{max} that is too large will include some solutes in the cluster that are actually in the matrix. Using a d_{max} that is too large may also incorrectly merge closely adjacent clusters. Values of d_{max} (and N_{min}) that are too small can result in incorrect classification of random fluctuation as clusters, and underestimate the number of solutes in larger clusters. Thus in all cases, a sensitivity analysis was performed to determine the most suitable values of d_{max} and N_{min}. The optimal d_{max}, based mainly on the solute separation distance distribution deviations from random, was found to be 0.50-0.60nm, with a corresponding N_{min} of 15-30 atoms. The maximum separation envelope of additional elements (L) and the erosion distance (E) were taken as equal to d_{max}, consistent with the less than or equal to recommendation in [53]. These values have been found to produce self-consistent results for a large RPV steel database. Note, however, lower L and E do not have a significant effect, and there is no absolutely "correct" values of these parameters that can be chosen. More details on the principles and practice of the APT technique, and selecting appropriate reconstruction parameters, can be found elsewhere [37,38,40]. As noted above, the Fe nominally in the precipitates was treated as an artifact and was removed when calculating the precipitate size and compositions [2,45–47]. After correction for detector efficiency, the sizes and volume fraction of the precipitates were determined from the number of solute atoms they contain, assuming a spherical morphology and an atom density equal to bcc Fe. Note, the nominal IVAS Fe content is also provided in the Table 2 below. N was calculated by dividing total identified clusters by the total APT tip volume. Clusters that intersect the tip surface were counted as half of a precipitate. The f was determined by dividing the number of solute atoms in all clusters by total number of atoms of a dataset.

2.3 Irradiation Hardening Measurements

Irradiation hardening was measured based on tensile, Vickers microhardness (H_v) and shear punch tests (SPT) [31]. In 7 out of the 9 alloys tensile data was available. For the other 2 alloys, the estimated $\Delta\sigma_y$ was taken as the average of that based on H_v and SPT $\Delta\sigma_y$. Procedures to convert the H_v and SPT to $\Delta\sigma_y$ are described in [31] and summarized below. The tensile and averaged H_v and SPT $\Delta\sigma_y$ are generally in good agreement.

At least three room temperature tensile tests on SS-J2 tensile specimens, with gauge sections 1.2 mm wide, 5 mm long, 0.5mm thick, were carried on a MTS 810 frame with a 1000lb load cell at a strain rate of 1.5×10^{-3}/s. A 0.2% offset was used to define the σ_y.

Vickers microhardness tests were performed on a modified LECO 400 series instrument, using a diamond pyramid indenter at a 500g load with a 10 second dwell time. The specimens were in the form of 3 mm discs, loaded in a multi-disc holder, and polished on a Buehler Vibromet with colloidal silica suspension down to 0.05µm. The spacing between indents was more than 3 times their size. The H_v was calculated by measuring the diagonal lengths of the indents with a 40x digital microscope. If the difference between two indent diagonal lengths was greater than 5%, the data was discarded. A minimum of 10 indents was made in each case, and the average and standard deviation of H_v were tabulated. Changes in Vickers hardness after irradiation ($\Delta H_v = H_{vi} - H_{vu}$) were used to estimate the corresponding changes in yield stress as $\Delta\sigma_y$ (MPa) $\approx 3.33*\Delta H_v$ (kg/mm^2) [45].

A semi-automated shear punch test tool, developed by UCSB, was used to measure the shear yield stress (τ_y) and maximum shear load (τ_m). Details describing the operation of the tool and its calibration can

be found in [31]. The SPT tool clamps round coupons, 8 to 20 mm in diameter (d) and 0.5 mm thick (t), between an upper punch plate assembly and die. A hydraulic actuator drives the 3 mm diameter (d_p) punch, and an in-line load cell provides the punch pressure (P) data. A lower die plate assembly extensometer measures the displacement (D) of the bottom of the disc being punched. The resulting P(D) curve manifests a quasi linear elastic region, followed by a non-linear plastic deviation of P with increasing D up to a maximum load (P_m). The shear yield pressure ($P_{\tau y}$) is determined by the intersection of a 0.9% parallel displacement from the elastic load line with the P(D) curve. The shear yield stress is defined as $\tau_y = P_{\tau y}/\pi d_p t$, where t is the local coupon thickness. A large tensile and SPT database for irradiated and unirradiated alloys was used to develop fitted relations between τ_y and σ_y. In the case of unirradiated alloys σ_{yu} is $\approx 1.81\tau_{yu}$, while for irradiated alloys σ_{yi} is $\approx 2.04\tau_{yi}$. The difference in the coefficient is associated with the effect of irradiation on reducing strain hardening. Thus, the SPT $\Delta\sigma_y$ is $\approx 2.04\tau_{yi} - 1.81\tau_{yu}$. Typically, 5 SPT were made on each 20 mm diameter disc, although more are possible, and retesting was carried out as needed in some cases.

3. Results

3.1 MNSP Characterization

Figure 1 shows typical solute maps for 4 irradiated alloys with 0.19 to 3.50 % Ni, 0.03 to 0.06% Cu, 0.80 to 1.34% Mn, and 0.39 to 0.49% Si. The volume fractions of the MNSPs visibly increase with increasing alloy Ni content. Table 2 summarizes the average APT bulk, matrix and MNSP compositions for the 9 alloys with systematic variations in bulk Ni and Mn and low <0.06% Cu and typical 0.44±0.05% Si contents. The measured bulk solute values are in reasonably good agreement with the nominal alloy compositions for Cu, Ni, and Si (see Table 1). However, the dissolved Mn is lower than the nominal value by $\approx$ 0.02 to 0.67%. The lower concentration, and inhomogeneous distribution of dissolved Mn, are primarily due to its sequestering in pre-existing coarse-scale $(Mn_{0.8}Fe_{0.2})_3C$, carbides [28].
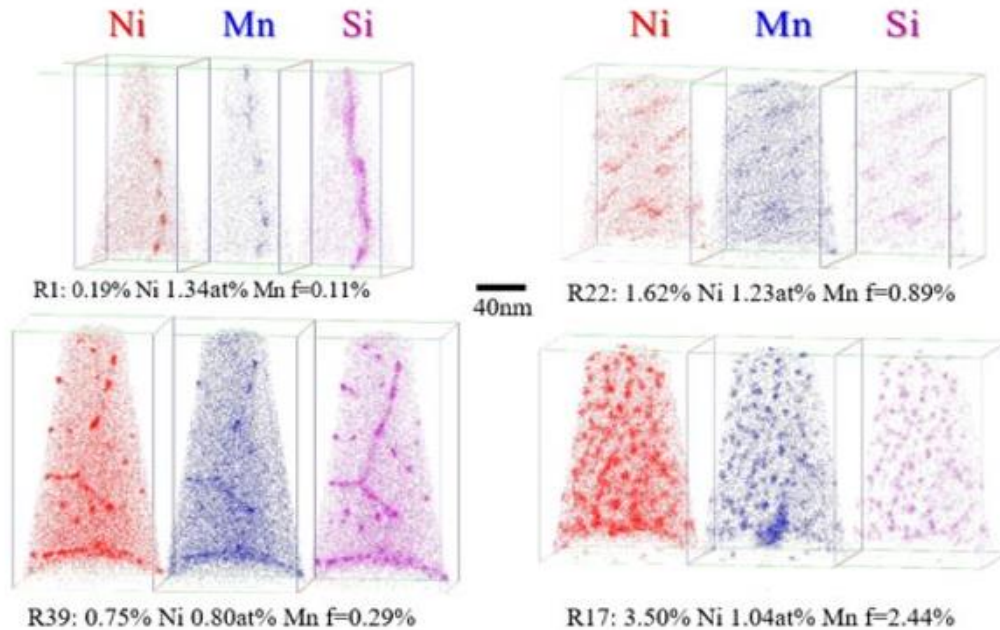

Figure 1. Solute maps for irradiated ASM alloys with systematically varying Ni from 0.19-3.30 at.% in steels with 0.03 to 0.06 % Cu, 0.80 to 1.34 % Mn and 0.39 to 0.49 % Si. All compositions are in at.%.

MNSPs are found in all cases at the high fluence of $\approx 1.4 \times 10^{20}$ n/cm^2 and 290°C. Note, well-defined CRPs form only at levels more than $\approx 0.07\%$ Cu, thus were not found in these steels [13,14,26]. However, Cu likely still has a catalyzing effect on the formation of MNSPs even at low levels [28], and all the MNSPs contain $\approx 1\%$ Cu, typically involving 8-32 atoms.

Table 2. Average APT bulk, matrix and precipitate compositions (at.%) for the 9 ASM alloys

Alloy	Bulk					Matrix					Precipitate				
	Cu	Ni	Mn	Si		Cu	Ni	Mn	Si		Cu	Ni	Mn	Si	Fe*
R1	0.05	0.24	0.24	0.49		0.04	0.21	0.22	0.44		1.5	37.1	14.6	46.8	58.2
R17	0.04	3.50	1.04	0.44		0.02	2.15	0.51	0.15		0.9	62.8	23.9	12.5	57.8
R19	0.05	1.80	0.24	0.47		0.05	1.55	0.22	0.35		1.0	64.4	5.1	29.4	64.3
R22	0.05	1.62	1.23	0.46		0.04	1.25	1.06	0.33		0.8	54.1	26.5	18.6	63.4
R26	0.04	3.40	0.22	0.39		0.04	2.91	0.19	0.25		0.9	73.5	4.7	20.8	58.1
R34	0.06	3.39	0.06	0.40		0.05	3.09	0.06	0.31		0.9	75.9	1.2	22.0	58.2
R35	0.04	0.19	1.34	0.46		0.04	0.17	1.27	0.44		1.3	26.4	42.4	30.0	65.1
R39	0.03	0.75	0.80	0.46		0.03	0.63	0.75	0.37		0.8	46.8	19.7	32.7	65.5
R48	0.05	3.45	0.48	0.42		0.04	2.58	0.32	0.19		1.0	69.2	12.5	17.2	58.6

*The nominal IVAS Fe found in all the MNSPs that is thought to largely be an artifact.

Table 3 summarizes the APT MNSP <d>, N and f. Multiple tips were measured and the corresponding +/- "uncertainties" in Table 3 reflect the variability between all the tips for the same alloy. The MNSP f increases synergistically with Ni and Mn. At high 3.5% Ni and 1.04% Mn f is 2.44%, while f is $\approx 0.44\%$ in the high 3.5% Ni, low 0.06% Mn steel. The f is very low at $\approx 0.08\%$ in the steel with only $\approx$ 0.24% Ni and Mn. These results demonstrate the strong synergistic effect of Ni and Mn on MNSPs.

Figure 1 also shows that the MNSPs in the low-medium Ni steels (0.3-0.8% Ni) are heterogeneously distributed, and are primarily ($\approx 70\%$) located on dislocations (and grain boundaries when present). Note, several of the low ≈ 0.3 % Ni alloy tips did not contain any MNSPs, due to their small APT sampling volume. These empty volumes were included in calculating N and f. The Mn, Ni, and especially Si, are highly segregated to dislocations. The role of solute segregation to dislocations, and dislocation loops, is important, and has been modeled [17,54], but we will not pursue this mechanism in detail further here. However, we note the models based on CALPHAD thermodynamics and radiation enhanced diffusion kinetics, reported by Ke et al., strongly support the critical role of heterogeneous MNSP nucleation in low to medium Ni steels [25]. The average MNSP compositions on dislocations are essentially the same as those observed in the matrix. The corresponding MNSP <d> and N are plotted in Figure 2 as a function of Ni for high and low Mn alloys. The average precipitate diameter, <d>, is $\approx 2.36 \pm 0.24$ nm, and is insensitive to both Ni and Mn. However, the MNSP N increases by a factor of ≈ 10 between ≈ 0.25 and 1.5 % Ni, and by a factor of 2-3 between low and high Mn steels. Between 1.5 and 3.5 %, the effect of Ni on N is weaker in the high Mn steel.

Table 3. Bulk Cu, Ni, Mn and Si compositions and APT precipitate $\langle d\rangle$, N and f

| Alloy	APT Bulk Composition (at%)				$\langle d\rangle$	+/-	N	+/-	f	+/-	10^6 atoms
	Cu	Ni	Mn	Si	(nm)	(nm)	(10^{23} m^{-3})	(10^{23} m^{-3})	(%)	(%)	
R1	0.05	0.24	0.24	0.49	2.31	0.02	0.92	0.40	0.08	0.15	9.8
R17	0.04	3.50	1.04	0.44	2.58	0.09	22.2	0.12	2.44	0.17	11.6
R19	0.05	1.80	0.24	0.47	2.47	0.03	5.07	0.09	0.42	0.04	17.8
R22	0.05	1.62	1.23	0.46	2.15	0.08	13.4	0.15	0.89	0.12	10.3
R26	0.04	3.40	0.22	0.39	2.46	0.04	8.37	1.69	0.69	0.11	48.9
R34	0.06	3.39	0.06	0.40	2.17	0.10	6.53	2.05	0.44	0.10	21.9
R35	0.04	0.19	1.34	0.46	2.22	0.03	1.83	0.27	0.11	0.08	20.8
R39	0.03	0.75	0.80	0.46	2.60	0.13	2.42	0.40	0.29	0.04	23.5
R48	0.05	3.45	0.48	0.42	2.29	0.08	21.2	0.60	1.41	0.22	38.9
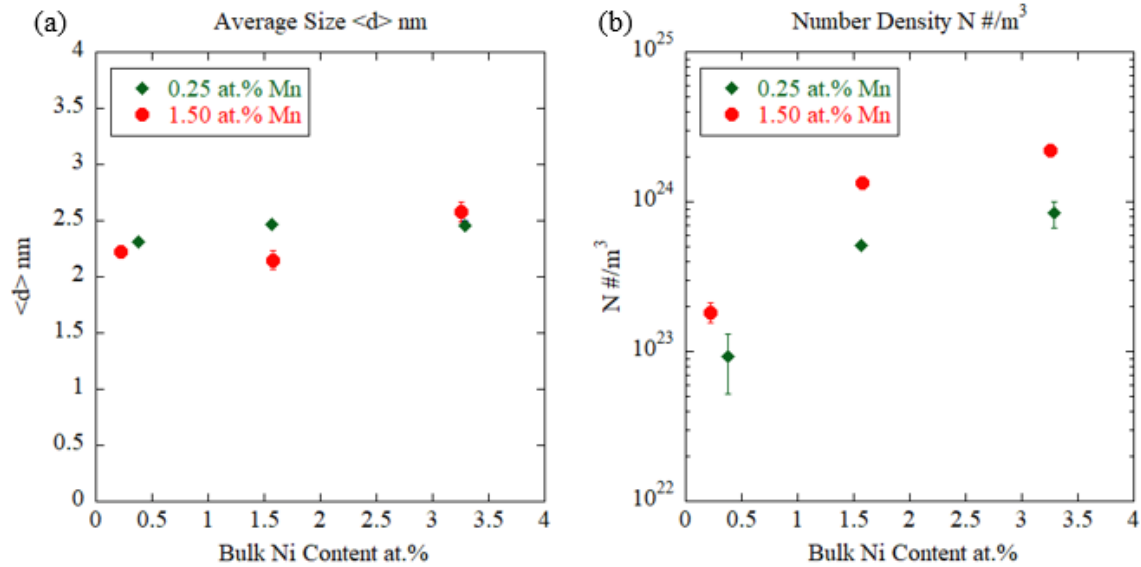
Figure 2. The effect of Ni at 0.25 and 1.5at%Mn (nominal) on the precipitate: a) average diameter, $\langle d\rangle$; and, b) number density, N.

Figure 3 shows a cross plot of f versus Ni at low, intermediate and high Mn. At low Mn (filled red circles), f is very low, as is the corresponding N. At low Ni, the effect of increasing Mn from 0.24% to 1.34% is minimal. In contrast, at high Mn (filled green diamonds), f increases approximately linearly with Ni up to ≈ 2.44%. The increase in f with Ni at ≈ 0.23 % Mn is less rapid, but is also approximately linear. The atoms maps in Figure 4a and b, and the f versus Mn cross plot in Figure 4c, demonstrate the profound and systematic effect of Mn in the 3.5% Ni steels. The increase in f with Mn is linear in the high Ni steels. As discussed in the next section, the reason is primarily related to phase composition selection, and corresponding solute balance requirements. That is, at very low Mn, the formation of Ni-Mn-Si phase compositions, which can incorporate the largest amount of Ni, is not possible. Indeed, at full decomposition, Ni ≈ 1-1.2(Mn+Si). Thus, the low f can be viewed as being due to Mn starvation. In this case, Si enriched phase compositions are selected, with Ni/Si ratios of ≈ 2 to 3. At high alloy 3.5% Ni and 1.04% Mn contents, 2.15% Ni remains dissolved in the matrix, while 3.09% Ni remains dissolved in the high 3.39%Ni, lower

0.06% Mn steel. The Ni-silicide type phase composition f is limited by the primary presence of only 2 elements, and a relatively low amount of bulk Si. Note, the increase in f from 0.44 to 0.69%, between the 0.06 and 0.25% Mn, is not primarily due to the precipitate Mn fraction; rather this is associated with a higher N in the latter case. This observation suggests that Mn also enhances Ni-silicide type phase composition nucleation rates. Similarly, the increase in f of 0.69% to 2.44%, between the 0.25 and 1.50 Mn, as shown in Figure 4, is associated with a $Ni_2(MnSi)$ type phase composition.
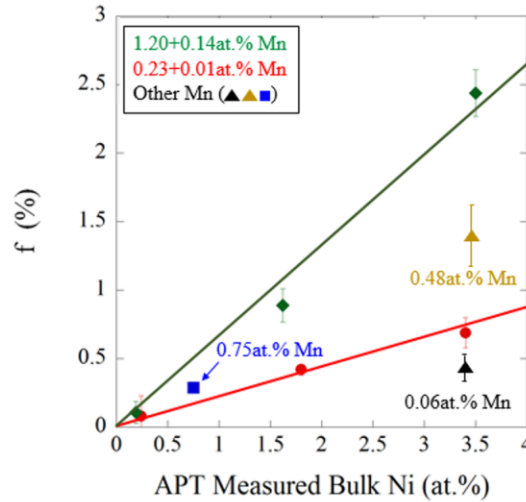
Figure 3. The effect of Ni on f for various Mn contents.
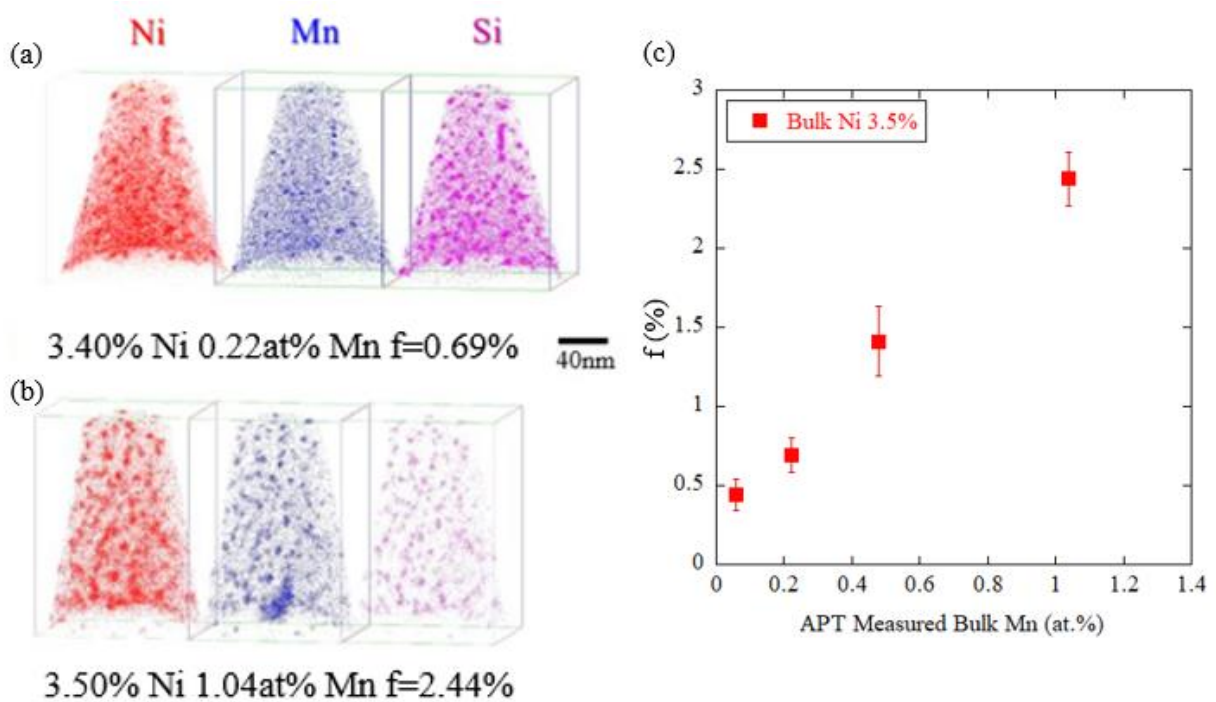
Figure 4. a) An APT solute map for a high 3.4% Ni, low 0.22% Mn steel; b) an APT solute map for a high 3.5% Ni, high 1.04% Mn steel; and c) a f versus bulk Mn cross plot for the high 3.5% Ni steels.

3.2 Irradiation Hardening

The isolated contribution of MNSPs to hardening is proportional to $\alpha(d)\sqrt{2f/d}$ [6], where $\alpha(d)$ is an obstacle strength factor. Since the precipitates are roughly the same size, it is expected that the dispersed dislocation obstacle hardening will scale with the $\sqrt{f}$. Figure 5 shows the measured irradiation yield stress increase ($\Delta\sigma_y$), summarized in Table 4, versus the $\sqrt{f}$ for the 9 alloys in this study. The filled circles are tensile data, while the unfilled squares are the average of the $\Delta\sigma_y$ estimates from the H_v and SPT. The half-filled squares are the cases where there is no tensile data. The least square fit slope is $\Delta\sigma_y \approx 300$ MPa/$\sqrt{f}$ (%). These results are reasonably consistent with previous studies with f between 0.2 and 1.25% based on isolated precipitate strength contributions of $520\sqrt{f}$ (MPa) that is root sum square superimposed with ≈ 175 MPa of unirradiated (and unchanged) obstacle strength contributions. However, the wide range of unirradiated yield stress values and microstructures for the steels in this study complicate a more detailed analysis.

Table 4 shows the bulk Ni and Mn compositions, and the precipitate Ni, Mn and Si compositions for the alloys in this study along with the corresponding f and $\Delta\sigma_y$. Figure 5 shows that $\Delta\sigma_y \approx 314\sqrt{f}$.

Table 4. Bulk Ni and Mn compositions and precipitate Ni, Mn and Si compositions (at%), along with f and $\Delta\sigma_y$

Alloy	Bulk (at.%)*		Precipitate (at.%)				f(%)	$\Delta\sigma_y$(MPa)
	Ni	Mn	Cu	Ni	Mn	Si		
R35	0.19	1.34	1.3	26.4	42.4	30.0	0.11	138
R1	0.24	0.24	1.5	37.1	14.6	46.8	0.08	100
R39	0.75	0.80	0.8	46.8	19.7	32.7	0.29	172
R22	1.62	1.23	0.8	54.1	26.5	18.6	0.89	291
R17	3.50	1.04	0.9	62.8	23.9	12.5	2.44	472
R19	1.80	0.24	1.0	64.4	5.1	29.4	0.42	235
R48	3.45	0.48	1.0	69.2	12.5	17.2	1.41	320+
R26	3.40	0.22	0.9	73.5	4.7	20.8	0.69	260
R34	3.39	0.06	0.9	75.9	1.2	22.0	0.44	169+

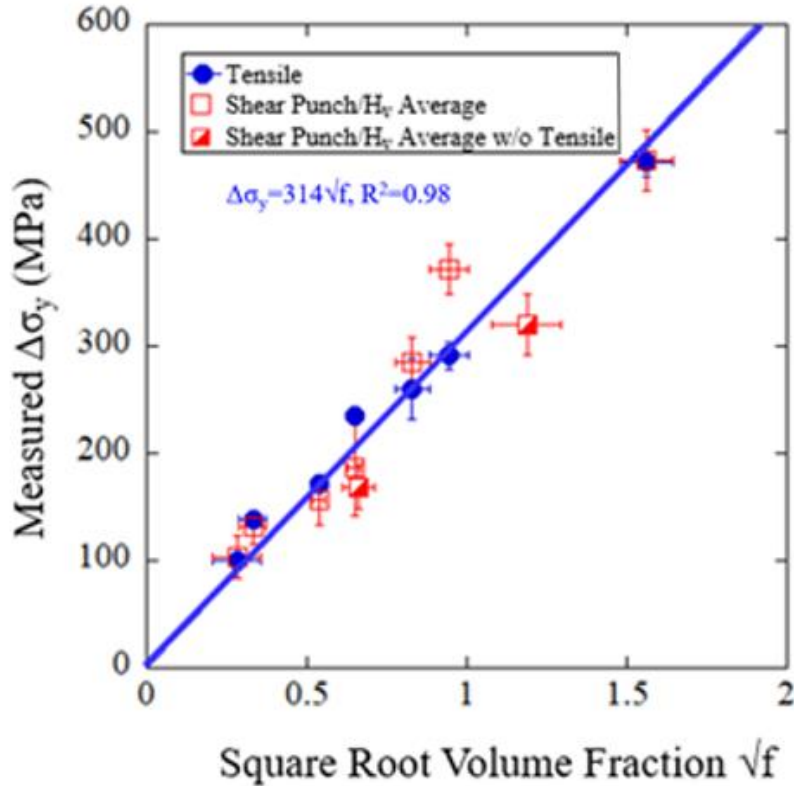*Plus 0.39 – 0.49% Si (at.%)   +Shear punch and microhardness $\Delta\sigma_y$ averaged

Figure 5. The measured $\Delta\sigma_y$ plotted as a function of the $\sqrt{f}$. Note the half-filled squares are cases where there is no tensile test data.

4. Discussion

The ternary Mn-Ni-Si _projection_ (see schematic quaternary figure insert) of the Fe-Mn-Ni-Si quaternary CALPHAD based phase diagram at 277°C is shown in Figure 6 [25,55]. Note there is no significant difference between the CALPHAD predictions at 277 and 290°C. The filled symbols are the average compositions of the precipitates in the various alloys. With one exception CALPHAD predicts that the precipitates do not contain Fe, consistent with experiment[2,47]. The exception is that, at very low Mn, CALPHAD predicts the formation of L1$_2$ Ni$_3$Fe phase. The open symbols specify the relative dissolved Mn-Ni-Si compositions in the unirradiated bulk matrix Fe-Mn-Ni-Si ferrite phase, and _they do not represent phases that actually lie in the ternary Mn-Ni-Si projection_. These relative bulk solute compositions are included _only to illustrate how they relate to the precipitate compositions_. Thus, the arrows should not be confused with compositions crossing phase boundaries, as the various tie lines are between the matrix (top of the tetrahedron – see insert) and the precipitate phases. Figure 6 shows that in 8 out of the 9 cases, the precipitate Si fraction is higher than the Si solute fraction in the unirradiated bulk. For typical RPV steel compositions (e.g., ≈ 0.7% Ni, > 1.0% Mn, and 0.4%-0.8% Si), CALPHAD predicts the predominant selection of G-phase (Mn$_6$Ni$_{16}$Si$_7$) or Γ_2 phase (Mn$_2$Ni$_3$Si).

Note, the CALPHAD database used in this case effectively either only predicts stoichiometric phases, or in some cases, a narrow phase field. However, the actual precipitate compositions vary somewhat with the corresponding alloy bulk composition, suggesting that there may be larger G and Γ_2-phase fields, which primarily extend towards higher Mn and lower Ni, over a range of Si. Such composition variations are to be expected, and can be the result of both the higher chemical potentials of the dissolved solutes in a matrix that is still supersaturated (e.g., the system is not fully decomposed in the equilibrium condition), as

12

well as composition dependent interface energy Gibbs-Thomson effects on the precipitates free energies. Thus, the free energy of the system is reduced over a range of precipitate compositions, even if the fully decomposed equilibrium phase is stoichiometric. This concept is illustrated in the Supplemental Material using a binary alloy analog. It is important to emphasize that, while the structural identities of both these phases have been confirmed by X-ray diffraction measurements for very high fluence irradiations [29], they have not yet been demonstrated for the MNSPs in this study. Thus, in this case, while we note compositional adjacency to various specific phases, we do not claim the precipitates have the corresponding crystal structures. Further, we cannot rule out the possibility that the precipitate compositions are slightly modified by radiation induced segregation.

As shown in Figure 7, the precipitate compositions vary in a way such that increases in Mn lead to decreases in Si, at a ratio of ≈ 0.4 to 0.6 lower Si/higher Mn numbers of atoms (that is a 10% increase in Mn lead to a 4 to 6% decrease in Si). These variations mirror the effect of bulk alloy Mn and Si variations. The individual supersaturated solute chemical potentials also explain why the precipitate compositions vary with the alloy bulk chemistry, and the observed tradeoff on the Mn-Si sublattice. The stoichiometric G and Γ_2 phases have (Mn +Si)/Ni ratios of ≈ 0.8 to 1, respectively. Given this rough Mn - Si tradeoff, it is to be expected that f would approximately scale with ≈ 1.6 to 2Ni at full decomposition. Indeed, in the nearly fully precipitated case, at very high fluence, $f \approx 1.38\text{Ni} + 0.49$ in the six core alloys with G and Γ_2 phases [28]. Again, this relation holds at nearly full decomposition, and only if the Mn alloy content is sufficient to form G and Γ_2 phases. At the lower fluence in this study, $f \approx 0.71\text{Ni} - 0.16$ for alloys with $\approx 1.2\%$ Mn. Note, that even when nearly fully decomposed, the nm scale precipitate f is less than the equilibrium values due to the Gibbs-Thomson effect.

To reiterate, Figure 6 simply intended to point out the location of the APT data on the ternary projection relative to possible phases. We made no claims that they are specific equilibrium phases, since we have not explicitly measured their crystal structures in these particular alloys. Rather, we simply attempt to note their compositional adjacencies (or lack thereof). For example, the compositions of three 1.7-3.5 Ni low < 0.25 Mn alloys (R19, 24 and 34) are clearly compositionally adjacent to Ni-silicide phases. The low Ni and Mn alloy (R1) is compositionally adjacent to the MnSi phase field. The low Ni, high Mn alloy (R35) is compositionally adjacent to the T8 phase field. One high Ni and Mn alloy (R22) is compositionally between G and Γ_2 phases. Two others with very high 3.5Ni and intermediate 0.5 to 1Mn alloys (R17, 39) are compositionally further from stoichiometric G or Γ_2 phase compositions, and have higher Ni contents ($\approx 12\%$ higher). Finally, the medium 0.7Ni intermediate 0.8Mn alloy has Ni similar to the Γ_2 phase field, but lower than the G-phase. All of this seems thermodynamically reasonable. Again note the composition of the nm-scale precipitates may be affected by supersaturated solutes and the interface energy that is, in turn, a function of the interface composition. Thus, small to modest deviations from nominal stoichiometric compound compositions are to be expected. Even if they have not been modeled, various stoichiometric phases may actually have finite composition fields. Further, as seen in Figure 6, and found in LMC studies of the B2 Mn-Ni-Si phase, Mn and Si are relatively interchangeable on their sublattice and thus react to the solutes chemical potential variations in the matrix. However, we have not made claims for this or that specific phase.
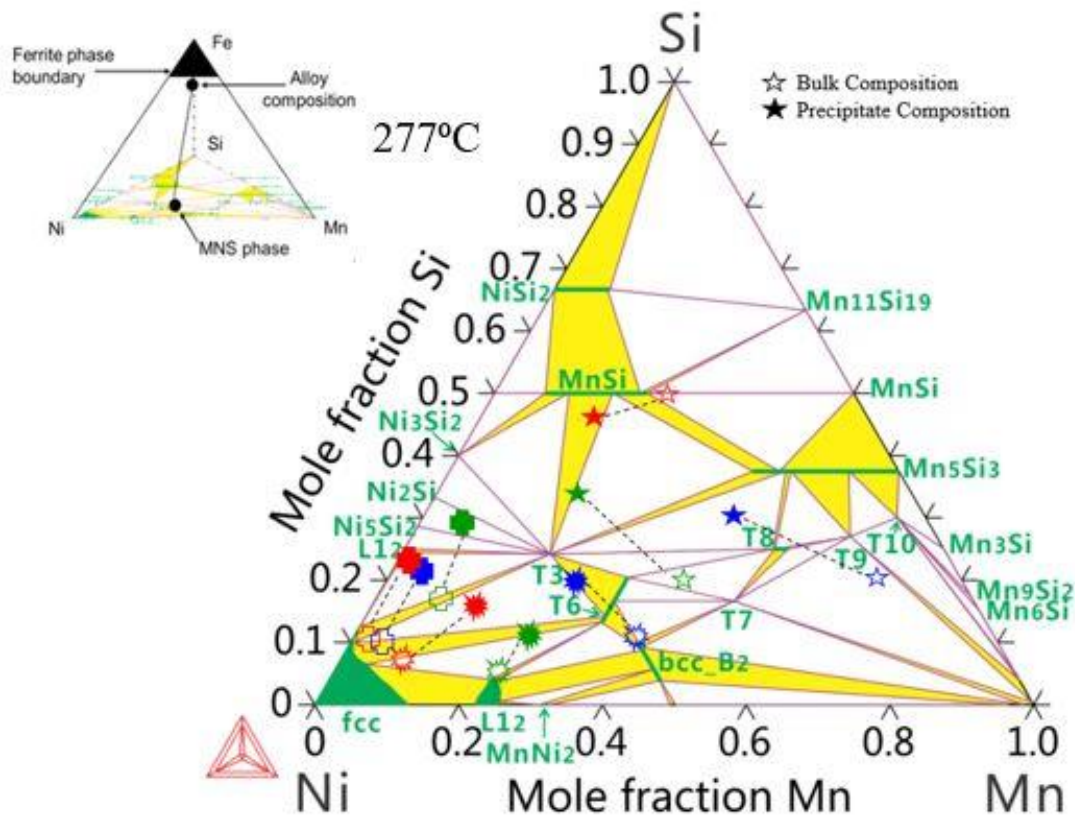
Figure 6. Bulk matrix and precipitate compositions plotted on the Mn-Ni-Si ternary projection of the Fe-Mn-Ni-Si phase diagram at 277°C. The APT measured precipitate compositions are filled symbols and the corresponding bulk alloy Mn-Ni-Si compositions are unfilled symbols [25,55]. Note, the open symbols are the relative fractions of dissolved solutes in the matrix ferrite phase, at the top of the tetrahedron, and they are not in the Mn-Ni-Si projection. The open symbols are only meant to show how the precipitate compositions relate to the solutes in the bulk. The dashed lines between the open and closed symbols are not tie lines.

While widely different alloy compositions result in different precipitate composition selection, it is useful to seek an alloy chemistry (composition) factor that correlates the precipitate f data for all 9 of the very diverse steels in this study. A natural choice is $Ni^n Mn^m$ (since Si is approximately constant), which reflects the thermodynamic reaction product driving precipitation (or an effective supersaturation) [25]. For example, for the Γ_2 phase the reaction is

$$3Ni(S) + 2Mn(S) + 1Si(S) \leftrightarrows Ni_3Mn_2Si$$
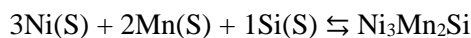
Here S indicates a dissolved solute. The corresponding reaction product is $K_\Gamma(T)[X_{ni}]^3[X_{mn}]^2[X_{si}]$. For the G phase the precipitation reaction is

$$16Ni(S) + 6Mn(S) + 7Si(S) \leftrightarrows Ni_{16}Mn_6Si_7$$
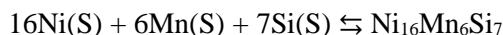
The corresponding reaction product is $K_G(T)[X_{ni}]^{16}[X_{mn}]^6[X_{si}]^7$. Here, the K(T) are the temperature dependent reaction constants. Reducing these exponents to the n/m ratios, gives 2.67 for the G-phase and 1.5 for the Γ_2 phase. Figure 8 shows a least square fit to f as a function of $Ni^n Mn^m$, that yields n ≈ 1.6 and m ≈ 0.8. Thus, the observed n/m ratio of 2, which is close to the average, which is 2.08 for stoichiometric

14

G and Γ_2 phases. Note, this should be considered an empirical observation, and a more detailed thermodynamic analysis will be needed to fully explain the relation, especially for Ni silicide phase compositions, in steels with low Mn contents.
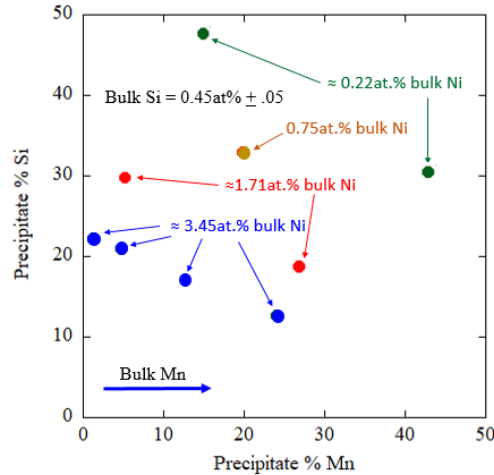

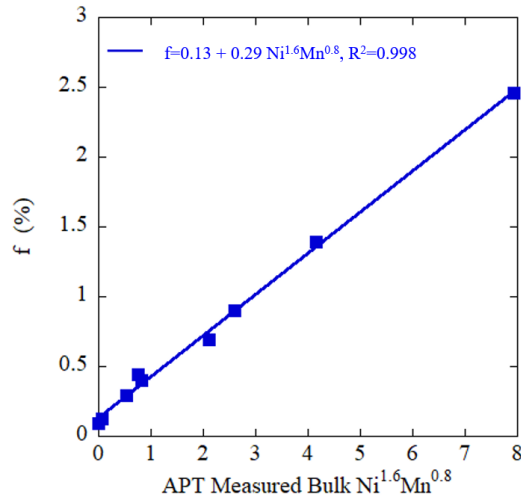Figure 7. Precipitate composition Mn-Si variations for different Ni groupings.

Figure 8. The $Ni^n Mn^m$ reaction product versus average f, and a least square fit to the data points for the 9 very compositionally diverse alloys in this study.

Perhaps most importantly, however, the results of this study clearly show that for the very high 3.5% Ni steels, low Mn greatly reduces the amount of precipitation, in a way that can be thermodynamically qualitatively understood. However, even at low Mn, Ni-silicide phases form in lower, but still significant, f. For example, f is $\approx 0.69\%$ for the 3.4% Ni, 0.22% Mn, 0.39% Si steel. We do not yet have APT data on steels with lower Si, but there is no significant effect of this element on $\Delta\sigma_y$ in the overall ATR-2 database. For example, in the case of 3.5% Ni steels with ≈ 0.25 Mn, the H_v based $\Delta\sigma_y$ actually decreases, but by only 21 MPa, in going from 0.38 to 1.28% Si; and for 3.5% Ni steels with ≈ 0.06 Mn, $\Delta\sigma_y$ decreases 3 MPa in going from 0.38 to 1.28% Si. These differences are insignificant and well within the data scatter.

Summary and Conclusions

This paper reports on the results of characterization of MNS precipitates by APT and irradiation hardening ($\Delta\sigma_y$) by tensile, shear punch and microhardness tests in specially prepared heats of compositionally tailored RPV-type steels, with a wide range of systematically varying Ni and Mn compositions and an approximately constant Si content, that were irradiated to a high fluence 1.4×10^{20} n/cm^2 at 290°C in the Advanced Test Reactor. Analysis of the data leads to the following conclusions.

- Significant volume fractions (f) of MNSPs form in all of the steels at the high ATR fluence.

- While Ni generally plays the strongest role in the formation of MNSPs, f and $\Delta\sigma_y$ increase synergistically and systematically with Mn, especially at higher Ni.

- In the absence of sufficient Cu and low to intermediate Ni, the MNS precipitates have difficulty nucleating homogeneously in a defect free matrix, and microstructural features such as network dislocations and irradiation induced interstitial loops act as heterogeneous nucleation sites.

- The wide range of compositions in the 9 alloys results in very different precipitate compositions - for example, near G ($Mn_6Ni_{16}Si_7$) or Γ_2 (Mn_2Ni_3Si) phases in alloys with 0.75% to 1.62% Ni with $\geq$ 0.8% Mn, versus Ni-silicide type compositions in alloys with very low $\leq$ 0.24 Mn and high $\approx$ 1.6 to 3.4% Ni. Note that, the G and Γ_2 phases have been identified at high fluence at typical RPV compositions, the specific phase structures not yet confirmed identified in this work.

- The Mn and Si in the precipitates roughly trade off depending on the alloy Mn content.

- At normal levels of > 1% Mn, very large MNS precipitate f form in 3.5% Ni advanced steels at high fluence.

- However, f decreases approximately linearly with the alloy Mn content, and is found to vary as $f \approx 0.13 + 0.3Ni^{1.6}Mn^{0.8}$.

- Precipitation hardening is much lower in high $\approx$ 3.5% Ni < 0.3% Mn steels due to Mn starvation.

- The $\Delta\sigma_y$ is well correlated with the $\sqrt{f}$ and can be understood based on dispersed barrier hardening models.

Acknowledgements

References

[1]   B. Zhang, F. Xue, S.L. Lu, Non-uniform phase separation in ferrite of a duplex stainless steel, Acta Mater. 140 (2017) 388–397. doi:10.1016/j.actamat.2017.08.044.

[2]   P.D. Edmondson, C.M. Parish, R.K. Nanstad, Using complimentary microscopy methods to examine Ni-Mn-Si-precipitates in highly-irradiated reactor pressure vessel steels, Acta Mater. 134 (2017) 31–39. doi:10.1016/j.actamat.2017.05.043.

[3]   Y. Matsukawa, T. Takeuchi, Y. Kakubo, T. Suzudo, H. Watanabe, H. Abe, T. Toyama, Y. Nagai, The two-step nucleation of G-phase in ferrite, Acta Mater. 116 (2016) 104–113. doi:10.1016/j.actamat.2016.06.013.

[4]   H. Leitner R. Schnitzer M. Schober et al, Precipitate modification in PH13-8 Mo type maraging steel, Acta Mater. 59 (2011) 5012–5022. doi:10.1016/j.actamat.2011.04.053.

[5]   W.W. Sun, R.K.W. Marceau, M.J. Styles, D. Barbier, C.R. Hutchinson, G phase precipitation and strengthening in ultra-high strength ferritic steels: Towards lean "maraging" metallurgy, Acta Mater. 130 (2017) 28–46. doi:10.1016/j.actamat.2017.03.032.

[6]   W. Martin, Micromechanisms in Particle-Hardened Alloys, Cambridge University Press, 1980.

[7]   K.C. Russell, L.M. Brown, A dispersion strengthening model based on differing elastic moduli applied to the iron-copper system, Acta Metall. 20 (1972) 969–974. doi:10.1016/0001-6160(72)90091-0.

[8]   Nuclear Energy Agency, Nuclear Power Plant Management and Longer-term Operation, (2006).

[9]   G.R. Odette, B.D. Wirth, D.J. Bacon, Multiscale-Multiphysics Modeling of Materials : Embrittlement of Pressure-Vessel Steels, MRS Bull. 26 (2001) 176–181. doi:10.1557/mrs2001.39.

[10]   G.R. Odette, G.E. Lucas, Embrittlement of nuclear reactor pressure vessels, JOM. 53 (2001) 18–22. doi:10.1007/s11837-001-0081-0.

[11]   G.R. Odette, R.K. Nanstad, Predictive reactor pressure vessel steel irradiation embrittlement models: Issues and opportunities, JOM. 61 (2009) 17–23. doi:10.1007/s11837-009-0097-4.

[12]   C. English, J. Hyde, Radiation Damage of Reactor Pressure Vessel Steels, Comprehensive Nuclear Materials, Elsevier, 2012. doi:10.1016/B978-0-08-056033-5.00087-2.

[13]   G.R. Odette, On the dominant mechanism of irradiation embrittlement of reactor pressure vessel steels, Scr. Metall. 17 (1983) 1183–1188. doi:10.1016/0036-9748(83)90280-6.

[14]   G.R. Odette, G.E. Lucas, Recent progress in understanding reactor pressure vessel steel embrittlement, Radiat. Eff. Defects Solids. 144 (1998) 189–231. doi:10.1080/10420159808229676.

[15]   R.E. Stoller, G.R. Odette, B.D. Wirth, Primary damage formation in bcc iron, J. Nucl. Mater. 251 (1997) 49–60. doi:10.1016/S0022-3115(97)00256-0.

[16]   E. Meslin, B. Radiguet, P. Pareige, C. Toffolon, A. Barbu, Irradiation-Induced Solute Clustering in a Low Nickel FeMnNi Ferritic Alloy, Exp. Mech. 51 (2011) 1453–1458. doi:10.1007/s11340-011-9476-1.

[17]   E. Meslin, A. Barbu, L. Boulanger, B. Radiguet, P. Pareige, K. Arakawa, C.C. Fu, Cluster-dynamics modelling of defects in a-iron under cascade damage conditions, J. Nucl. Mater. 382 (2008) 190–196. doi:10.1016/j.jnucmat.2008.08.010.

[18]   E. Meslin, B. Radiguet, M. Loyer-Prost, Radiation-induced precipitation in a ferritic model alloy: An experimental and theoretical study, Acta Mater. 61 (2013) 6246–6254. doi:10.1016/j.actamat.2013.07.008.

[19]   R. Ngayam-Happy, C.S. Becquart, C. Domain, L. Malerba, Formation and evolution of MnNi clusters in neutron irradiated dilute Fe alloys modelled by a first principle-based AKMC method, J. Nucl. Mater. 426 (2012) 198–207. doi:10.1016/j.jnucmat.2012.03.033.

[20]   P. Auger, P. Pareige, S. Welzel, J.-C. Van Duysen, Synthesis of atom probe experiments on irradiation-induced solute segregation in French ferritic pressure vessel steels, J. Nucl. Mater. 280 (2000) 331–344. doi:10.1016/S0022-3115(00)00056-8.

[21]   J.T. Buswell, W.J. Phythian, R.J. McElroy, S. Dumbill, P.H.N. Ray, J. Mace, R.N. Sinclair, Irradiation-induced microstructural changes, and hardening mechanisms, in model PWR reactor pressure vessel steels, 225 (1995) 196–214. doi:10.1016/0022-3115(95)00026-7

[22]   M.K. Miller, K.F. Russell, Embrittlement of RPV steels: An atom probe tomography perspective, J. Nucl. Mater. 371 (2007) 145–160. doi:10.1016/j.jnucmat.2007.05.003.

[23]   G.R. Odette, On the ductile to brittle transition in martensitic stainless steels — Mechanisms, models and structural implications, J. Nucl. Mater. 212–215 (1994) 45–51. doi:10.1016/0022-3115(94)90032-9.

[24]   D. A. Curry, J. F. Knott, Effect of Microstructure on Cleavage Fracture Toughness in Mild Steel, Met. Sci. 13 (1979) 341–345. doi:10.1179/msc.1979.13.6.341

[25]   H. Ke, P. Wells, P.D. Edmondson, N. Almirall, L. Barnard, G.R. Odette, D. Morgan, Thermodynamic and kinetic modeling of Mn-Ni-Si precipitates in low-Cu reactor pressure vessel steels, Acta Mater. 138 (2017) 10–26. doi:10.1016/j.actamat.2017.07.021.

[26]   E.D. Eason, G.R. Odette, R.K. Nanstad, T. Yamamoto, A Physically Based Correlation of Irradiation-Induced Transition Temperature Shifts for RPV Steels, (2006). http://www.info.ornl.gov/sites/publications/files/Pub2592.pdf.

[27]   G.R. Odette, T. Yamamoto, D. Klingensmith, On the effect of dose rate on irradiation hardening of RPV steels, Philos. Mag. 85 (2005) 779–797. doi:10.1080/14786430412331319910.

[28]   P.B. Wells, T. Yamamoto, B. Miller, T. Milot, J. Cole, Y. Wu, G.R. Odette, Evolution of manganese–nickel–silicon-dominated phases in highly irradiated reactor pressure vessel steels, Acta Mater. 80 (2014) 205–219. doi:10.1016/j.actamat.2014.07.040.

[29]   D.J. Sprouster, J. Sinsheimer, E. Dooryhee, S.K. Ghose, P. Wells, T. Stan, N. Almirall, G.R. Odette, L.E. Ecker, Structural characterization of nanoscale intermetallic precipitates in highly neutron irradiated reactor pressure vessel steels, Scr. Mater. 113 (2016) 18–22. doi:10.1016/j.scriptamat.2015.10.019.

[30]   S. Shu, P.B. Wells, N. Almirall, G.R. Odette, D.D. Morgan, Acta Materialia Thermodynamics and kinetics of core-shell versus appendage co- precipitation morphologies : An example in the Fe-Cu-Mn-Ni-Si system, Acta Mater. 157 (2018) 298–306. doi:10.1016/j.actamat.2018.07.037.

[31] G.R. Odette, T. Yamamoto, P.B. Wells, N. Almirall, K. Fields, D. Gragg, R. Nanstad, M.A. Sokolov, J.P. Robertson, Update on the ATR-2 Reactor Pressure Vessel Steel High Fluence Irradiation Project, Light Water React. Sustain. Progr. Milestone Rep. (2016).

[32] M.G. Burke, R.J. Stofanak, J.M. Hyde, C.A. English, W.L. Server, Microstructural aspects of irradiation damage in A508 Gr 4N forging steel: Composition and flux effects, J. ASTM Int. 1 (2002) 1–14. doi:10.1520/JAI11773.

[33] G. Wire, W. Beggs, T. Leax, Evaluation of irradiation embrittlement of A508 Gr 4N and comparison to other low-alloy steels, in: 21st Int. Symp. Eff. Radiat. Mater., 2002: pp. 179–193. doi:10.1520/STP11227S.

[34] T. Leax, Temperature dependence and variability of fracture toughness in the transition regime for A508 grade 4N pressure vessel steel, 5th Int. ASTM/ESIS Symp. Fatigue Fract. 3 (2005) 1–20. doi:10.1520/JAI13230.

[35] S. Wu, H. Jin, Y. Sun, E. Al., Critical cleavage fracture stress characterization of A508 nuclear pressure vessel steels, Int. J. Press. Vessel. Pip. 123 (2014) 92–98. doi:10.1016/j.ijpvp.2014.08.003.

[36] M. Kim, S. Park, B. Lee, K. Lee, Comparison of Fracture Properties in SA508 Gr.3, Gr.4N high strength low alloy steels for advanced pressure vessel materials, Int. J. Press. Vessel. Pip. 131 (2015) 60–66. doi:10.1016/j.ijpvp.2015.04.010.

[37] S.P. Gault, B., Moody, M.P., Cairney, J.M., Ringer, Atom Probe Microscopy, 2012.

[38] M.K. Miller, Atom Probe Tomography, Kluwer Academic/Plenum Publishers, 2000.

[39] E.A. Marquis, Atom probe tomography applied to the analysis of irradiated microstructures, J. Mater. Res. 30 (2015) 1–9. doi:10.1557/jmr.2014.398.

[40] B. Gault, F. De Geuser, L.T. Stephenson, M.P. Moody, B.C. Muddle, S.P. Ringer, Microscopy Microanalysis Estimation of the Reconstruction Parameters for Atom Probe Tomography, Microsc. Microanal. 14 (2008) 296–305. doi:10.1017/S1431927608080690.

[41] E.A. Marquis, J.M. Hyde, Applications of atom-probe tomography to the characterisation of solute behaviours, Mater. Sci. Eng. R Reports. 69 (2010) 37–62. doi:10.1016/j.mser.2010.05.001.

[42] K. Lindgren, K. Stiller, P. Efsing, M. Thuvander, On the Analysis of Clustering in an Irradiated Low Alloy Reactor Pressure Vessel Steel Weld, Microsc. Microanal. 23 (2017) 376–384. doi:10.1017/S1431927617000162.

[43] K. Lindgren, M. Boåsen, K. Stiller, P. Efsing, M. Thuvander, Evolution of precipitation in reactor pressure vessel steel welds under neutron irradiation, J. Nucl. Mater. 488 (2017) 222–230. doi:10.1016/j.jnucmat.2017.03.019.

[44] J.M. Hyde, M.G. Burke, G.D.W. Smith, P. Styman, H. Swan, K. Wilford, Uncertainties and assumptions associated with APT and SANS characterisation of irradiation damage in RPV steels, J. Nucl. Mater. 449 (2014) 308–314. doi:10.1016/j.jnucmat.2013.07.029.

[45] P.B. Wells, The Character and Stability of Mn-Ni-Si Precipitates in Reactor Pressure Vessel Steels [PhD Thesis], Univ. Calif. St. Barbara (2015).

[46]   N.J. Cunningham, Study of the Structure, Composition, and Stability of Y-Ti-O nm-Scale Features in Nano-Structured Ferritic Alloys [PhD Thesis], Univ. Calif. St. Barbara (2012).

[47]   S. Shu, B.D. Wirth, P.B. Wells, D.D. Morgan, G.R. Odette, Multi-technique characterization of the precipitates in thermally aged and neutron irradiated Fe-Cu and Fe-Cu-Mn model alloys: Atom probe tomography reconstruction implications, Acta Mater. 146 (2017) 237–252. doi:10.1016/j.actamat.2017.12.006.

[48]   P. Pareige, C. Hatzoglou, B. Radiguet, Experimental artefacts occurring during atom probe tomography analysis of oxide nanoparticles in metallic matrix: Quantification and correction, J. Nucl. Mater. 492 (2017) 279–291. doi:10.1016/j.jnucmat.2017.05.008.

[49]   A. Morley, G. Sha, S. Hirosawa, A. Cerezo, G.D.W. Smith, Determining the composition of small features in atom probe: bcc Cu-rich precipitates in an Fe-rich matrix, Ultramicroscopy. 109 (2009) 535–540. doi:10.1016/j.ultramic.2008.09.010.

[50]   W.R. McKenzie, E.A. Marquis, P.R. Munroe, Focused Ion Beam Sample Preparation for Atom Probe Tomography, Microsc. Sci. Technol. Appl. Educ. 3 (2010) 1800–1810. http://www.formatex.info/microscopy4/1800-1810.pdf.

[51]   J.M. Hyde, C.A. English, An Analysis of the Structure of Irradiation induced Cu-enriched Clusters in Low and High Nickel Welds, MRS Proc. 650 (2000) R6.6. doi:10.1557/PROC-650-R6.6.

[52]   L.T. Stephenson, M.P. Moody, P. V. Liddicoat, S.P. Ringer, New Techniques for the Analysis of Fine-Scaled Clustering Phenomena within Atom Probe Tomography (APT) Data, Microsc. Microanal. 13 (2007) 448–463. doi:10.1017/S1431927607070900.

[53]   J.M. Hyde, E.A. Marquis, K.B. Wilford, T.J. Williams, A sensitivity analysis of the maximum separation method for the characterisation of solute clusters., Ultramicroscopy. 111 (2011) 440–447. doi:10.1016/j.ultramic.2010.12.015.

[54]   G. Bonny, D. Terentyev, E.E. Zhurkin, L. Malerba, Monte Carlo study of decorated dislocation loops in FeNiMnCu model alloys, J. Nucl. Mater. 452 (2014) 486–492. doi:10.1016/j.jnucmat.2014.05.051.

[55]   W. Xiong, H. Ke, P.B. Wells, L. Barnard, R. Krishnamurthy, G.R. Odette, D. Morgan, Thermodynamic models of low temperature Mn-Ni-Si precipitation in reactor pressure vessel steels, Mater. Res. Soc. Commun. 4 (2014) 101–105. doi:10.1557/mrc.2014.21.

Precipitation and Hardening in Irradiated Low Alloy Steels with a Wide Range of Ni and Mn Compositions

N. Almirall[1], P.B. Wells[1], T. Yamamoto[1], K. Wilford[2], T. Williams[2], N. Riddle[2] and G.R. Odette[1]

[1]University of California, Santa Barbara

[2]Rolls-Royce

Discussion of Equilibrium Phases

The nm-scale precipitates cannot be expected to have the same composition as bulk equilibrium phases due to the Gibbs-Thomson effect and compositionally dependent interface energies, even if their structure phase is the same as that of the bulk equilibrium phase. Further, in this case the alloys are not fully decomposed; that is they remain supersaturated. Thus the chemical potentials remain higher in solution than at equilibrium. For any reasonable intermetallic free energy curve, this provides thermodynamic access to a wider range of compositions, that still reduce the free energy G. This is schematically illustrated in Figure 1Sa for a binary with a terminal phase – AB intermetallic phase. The green line represents the equilibrium condition while the red line is for the partially decomposed state. The Gibbs-Thomson effect shifts the G-curve up in energy and typically to lower X_B due to the composition dependence of the interface energy (red dashed line). Thus a range of compositions is thermodynamically accessible. Further, the precipitate composition would be expected to vary with the chemical potential of the various dissolved solutes as governed by Henry's law. That is more dissolved/supersaturated matrix Ni would lead to more precipitate Ni (or Mn or Si). Figure 1Sb APT shows the range of compositions narrows with increasing precipitate size as would be expected from the considerations outlined above. Note that in this case the composition of the precipitates are 10% lower in Ni and 10% higher in Mn + Si (that trade-off), which does not seem that large a deviation.
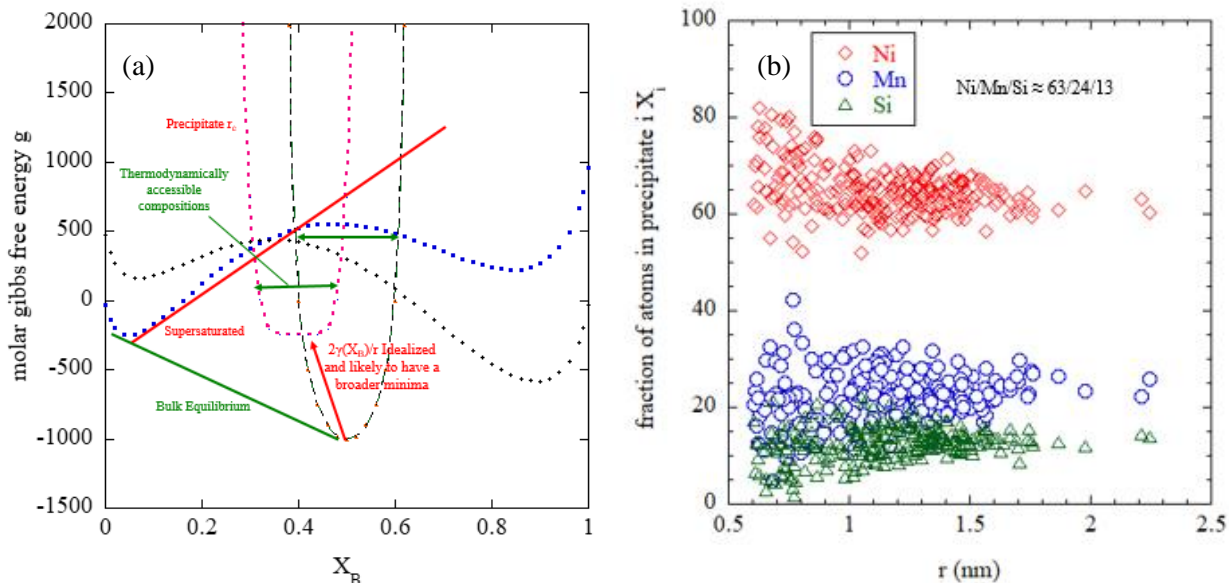

Figure 1S. (a) Molar gibbs free energy curves for a binary with an AB intermetallic phase (b) APT spread in 3.5% Ni 1.0at% Mn alloy of precipitate composition plotted against precipitate radius